Table S1. IR-spectra (cm^{-1} in KBr pellets) of starting compounds and salts **1-3**.

	HATNA	$Mn^{II}(dedtc)_2$	$Mn^{II}(acac)_2$	cryptand	$C_6H_4Cl_2$	C_6H_{14}	$\{Mn^{II}(dedtc)_2 \cdot HATNA\}$ (**1**)	$\{(K^+)(crypt)\}_2[\{Mn^{II}(dedtc)_2\}_3(HATNA)]^{2-} \cdot 2C_6H_4Cl_2$ (**2**)	$\{(K^+)(crypt)\}_2[\{Mn^{II}(acac)_2\}_3(HATNA)]^{2-} \cdot 2C_6H_4Cl_2 \cdot C_6H_{14}$ (**3**)
HATNA	413m						412m*	410w*	406m*
	501w						506w*	504w*	504w*
	541w						-	522w	531w
	606m						608w*	618s	602w*
	757s						753s*	751s*	755m*
	771m						-	780m	779sh*
	802w						843m	840m	831w
	1001w						994m*	997m*	1010m
	1020w						1042w	1031w	-
	1078s						1079s*	1076sh*	1077sh*
	1129w						1140s	1134m*	1131m*
	1236w						-	1239sh*	1216w
	1339m						1342w*	1318m	1317m
	1364m						1366m*	1371w	1355m
	1495m						1485s	1466s	-
	1521w						1523sh*	1483sh	1510s
	1611w						1612w*	1633w	1600s
	3056w						3056w*	3060w*	3064w*
$Mn^{II}L$							$Mn^{II}(dedtc)_2$	$Mn^{II}(dedtc)_2$	$Mn^{II}(acac)_2$
							406sh*	400w*	406m
		406w	419w				450w*	456w	504w*
		446m	501w				565w	567w	571w*
		544m	564w				653w	657w	602w*
		646w	598w				753s	751s	779sh*
		769w	775w				911m*	914w*	831w*
		918w	839m				994m	997m	914w*
		1013w	911m				1211s	1213m	1010m
		1192w	985m				1267s	1261s	-
		1252s	1066w				1366m*	1354m	1077sh*
		1362s	1074m				1523sh	1483sh	1104s*
		1506s	1094w				1612w	-	1131m*
		1601s	1139s						1189w
			1207s						1259m*
			1266s						-
			1272s						1300sh*
			1297m						1355m*
			1356m						-
			1427s						1411s
			1462w						1467m*
			1485s						1510s
crypt				cryptand				cryptand	cryptand
				476w				471w*	470w*
				528w				522w*	531w*
				735m				751s	755m
				922m				932w	932sh
				948w				950m*	950m*
				982m				997m	1010m
				1071m				1076sh*	1077sh*
				1100s				1103s*	1104s*
				1127s				1134m*	1131m*
				1213w				1213m*	1216w*
				1295m				1300w*	1300sh*
				1329m				1318m	1317m
				1360s				1354m*	1355m*
				1446m				-	-
				1462m				1466s*	1467m*
				1490w				1483sh*	1510s
				2790w				2818w	2813w
				2877w				2883m	2882m*
				2943w				2928w	2959w

solvent					$C_6H_4Cl_2$ 657w 748s 1030m 1122m 1453m	 C_6H_{14} 722s 758w 882m 1060m 1342m 1373s 1460s		$C_6H_4Cl_2$ 657w 751s* 1031w* 1134m 1466s	$C_6H_4Cl_2$ 651w* 755m* 1010m 1131m 1467m C_6H_{14} - 755m* 885sh* 1077sh 1355m 1411s 1467m*

*****bands coincide, w - weak, m - middle, s – strong, sh- shoulder .

Table S2. IR-spectra (cm^{-1} in KBr pellets) of starting compounds and salts **4-5**.

	HATNA	HATA	CVCl	cryptand	$C_6H_4Cl_2$	$(CV^+)_2\{(Mn^{II}Cl_2)_3(HATA)\}^{2-}\cdot 4C_6H_4Cl_2$ (**4**)	$\{(K^+)(crypt)\}_{23}\{(Mn^{II}I_2)_3(HATNA)\}^{3-}\cdot 5C_6H_4Cl_2$ (**5**)
HAT	HATNA	HATA				HATA	HATNA
	413m	420w				418w*	412w*
	501w	468w				473w*	504w*
	541w	493w				500w*	524w
	606m	589w				603w	625s
	757s	620w				645w	753m*
	771m	742s				758w	-
	802w	840w				837m*	790w
	1001w	876m				864w	994s*
	1020w	1076s				1065w	1032sh
	1078s	1170w				1172s*	1077w*
	1129w	1254w				1228w	1131m*
	1236w	1286w				1298w	1256m
	1339m	1372w				1363s	1315sh
	1364m	1403s				1398w*	1355m
	1475w	1530w				1525w*	1467m*
	1495m	1550w				1583s	-
	1521w	1630m				-	1557s
	1611w	2860w				2861w*	-
	3056w	2921w				2921w*	3060w*
Cat^+			CV^+	cryptand		CV^+	cryptand
			419w	476w		418w*	457w
			501w	528w		500w*	524w*
			564w	735m		558w*	753m
			598w	922m		603w*	903w
			775w	948w		758w	950s*
			839m	982m		837m*	994s
			911m	1038w		911w*	1032sh*
			985m	1071m		943m	1077w*
			1066w	1100s		1065w*	1102s*
			1074m	1127s		-	1131m*
			1094w	1213w		1122w	1201w
			1139s	1295m		1146sh	1300m*
			1207s	1329m		1186w	1315sh
			1266s	1360s		1228w	1355m*
			1272s	1446m		-	1443w*
			1297m	1462m		1298w*	1467m*
			1340w	1490w		-	-
			1356m	2790w		1363s*	2816w
			1378m	2877w		1398w	2881m*
			1427s	2943w		1412w	2957w
			1452w			1457m*	
			1462w			1473w	
			1485s			1506w	
$C_6H_4Cl_2$					$C_6H_4Cl_2$	$C_6H_4Cl_2$	$C_6H_4Cl_2$
					657w	668w	668w*
					748s	744w*	753m*
					1030m	1030w*	1032sh*
					1122m	1122w*	1131m
					1453m	1457m*	1467m

*****bands coincide, w - weak, m - middle, s – strong, sh- shoulder .

IR-spectra of the complexes.

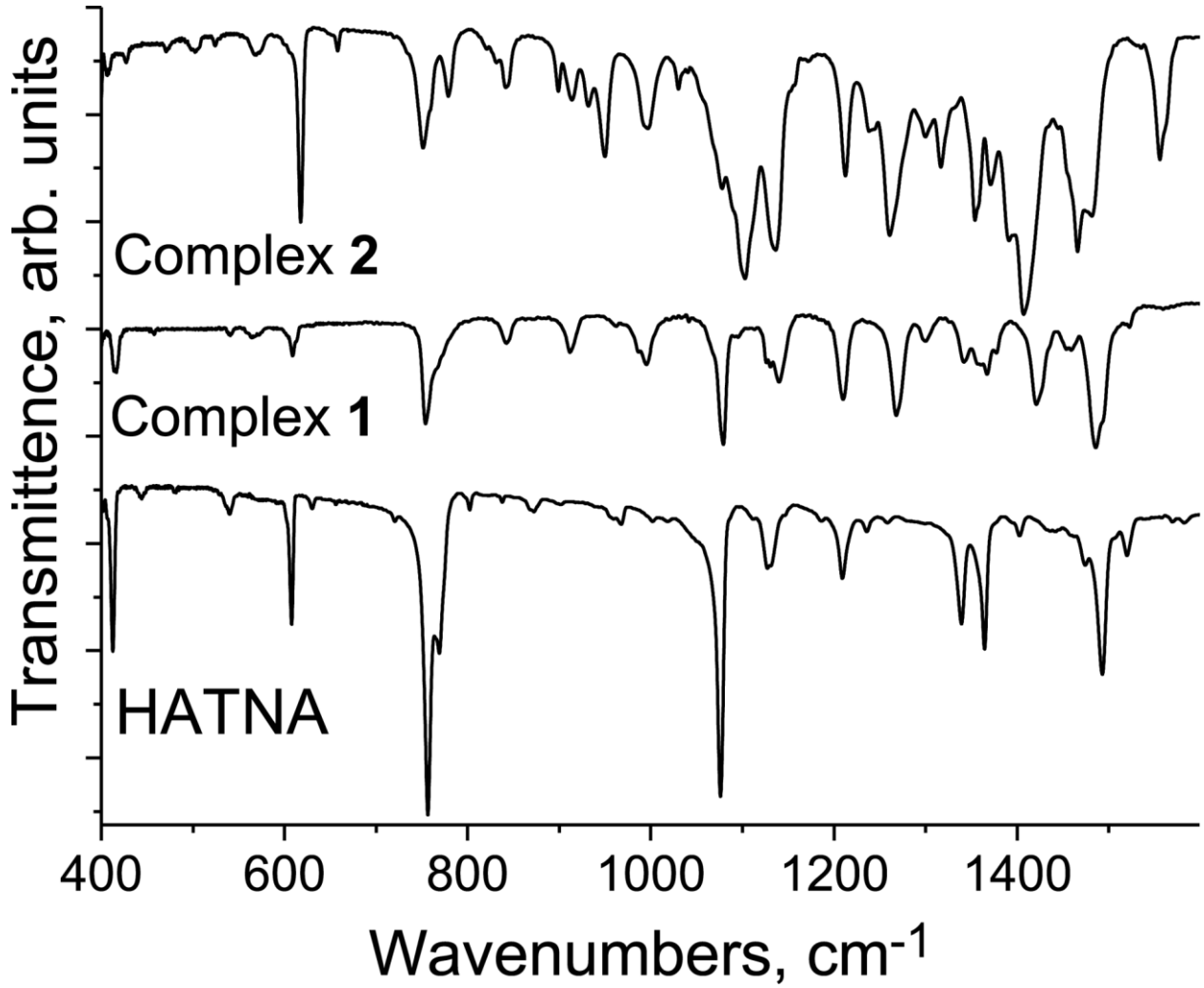

Figure S1. IR-spectrum of starting HATNA and the spectra of $\{Mn^{II}(dedtc)_2(HATNA)\}$ (**1**) and $\{(K^+)(crypt)\}_2[\{Mn^{II}(dedtc)_2\}_3(HATNA)]^{2-}\cdot 2C_6H_4Cl_2$ (**2**) in KBr pellets. Pellets for **1** and **2** were prepared in anaerobic conditions.

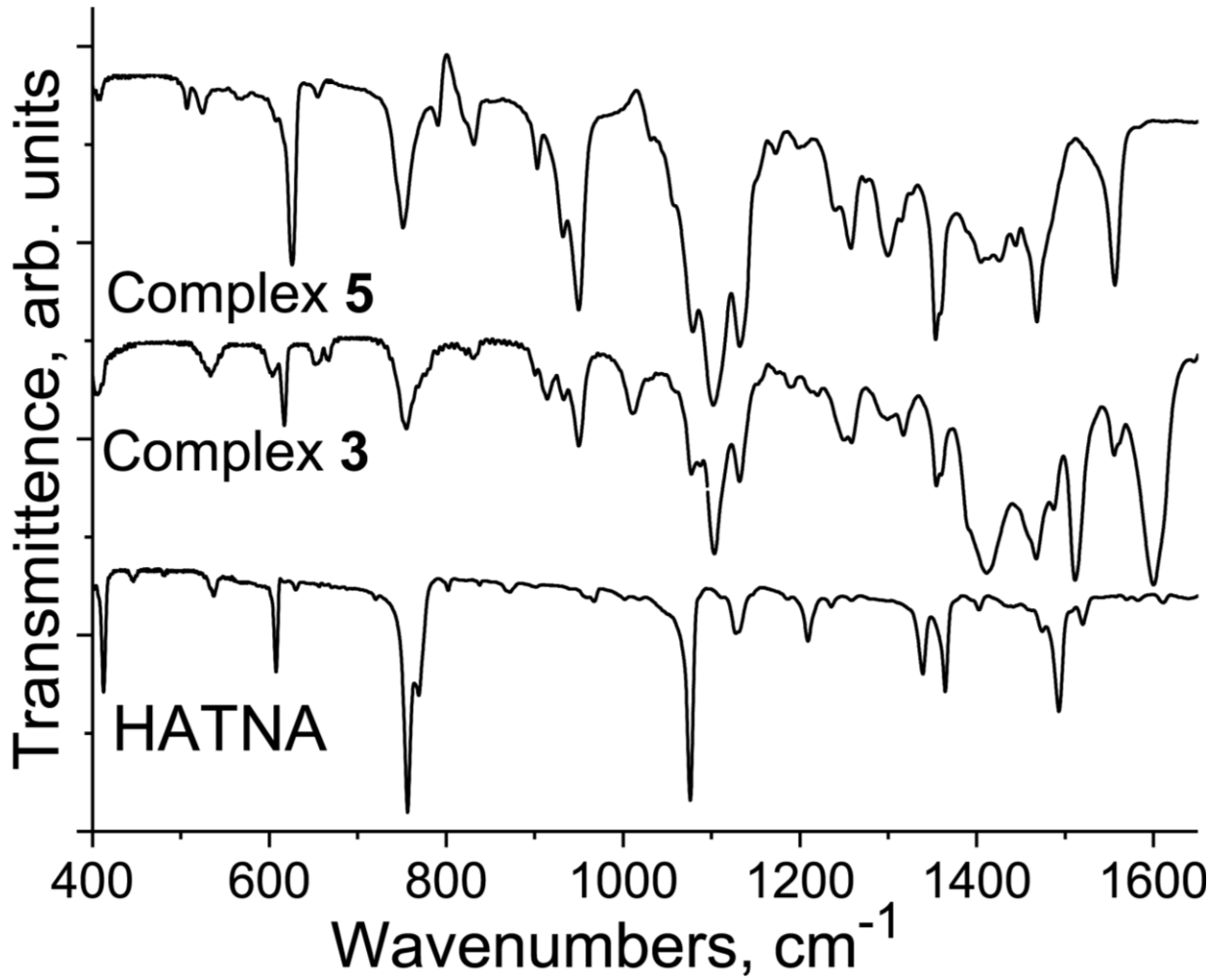

Figure S2. IR-spectrum of starting HATNA and the spectra of $\{(K^+)(crypt)\}_2[\{Mn^{II}(acac)_2\}_3(HATNA)\}^{2-}\cdot 2C_6H_4Cl_2\cdot C_6H_{14}$ (**3**) and $\{(K^+)(crypt)\}_3\{(Mn^{II}I_2)_3(HATNA)\}^{3-}\cdot 5C_6H_4Cl_2$ (**5**) in KBr pellets. Pellets for **3** and **5** were prepared in anaerobic conditions.

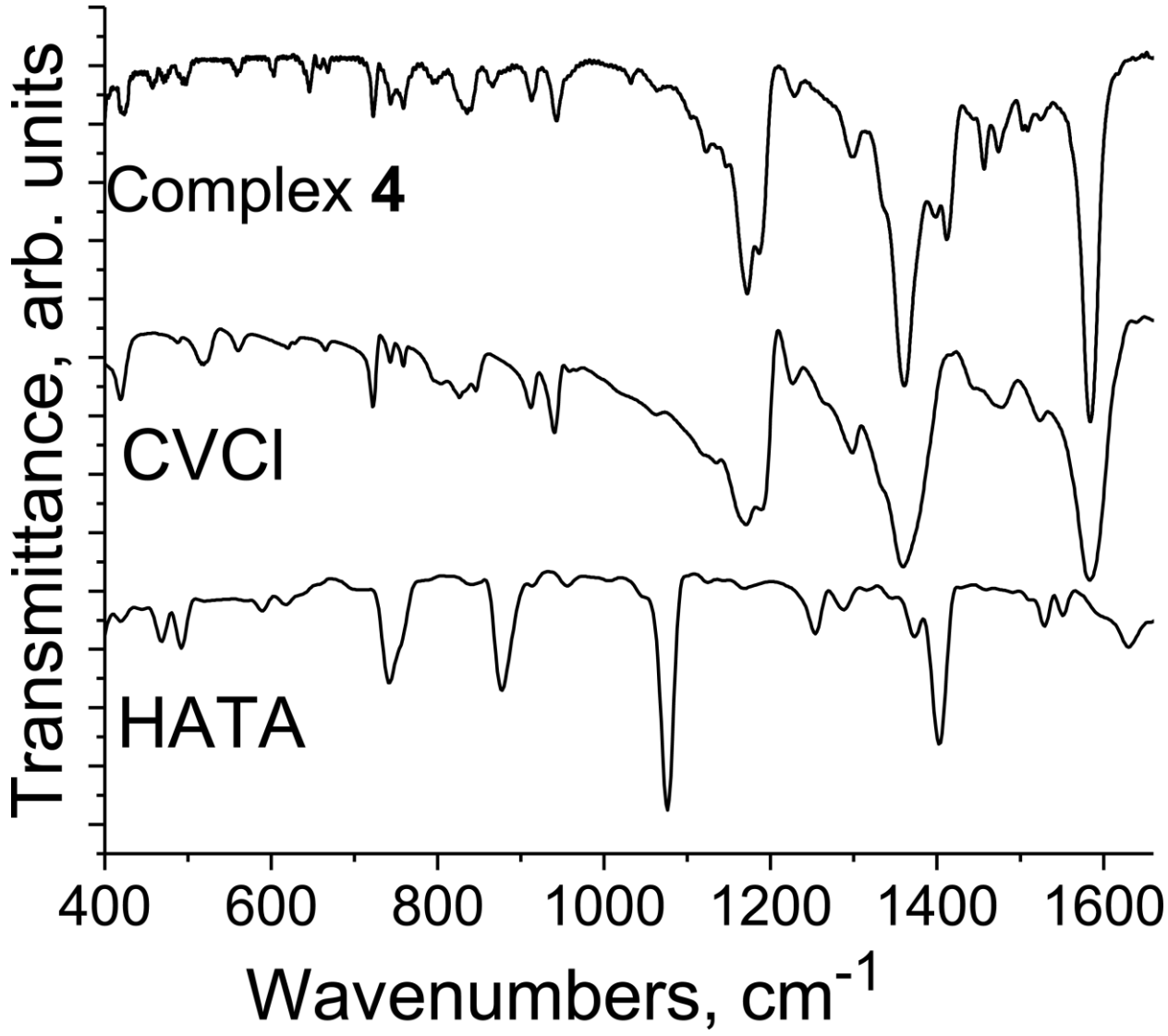

Figure S3. IR-spectra of starting HATA, salt CVCl and complex $(CV^{+})_2\{(Mn^{II}Cl_2)_3(HATA)\}^{2-}\cdot 4C_6H_4Cl_2$ (**4**) in KBr pellets. Pellet for **4** was prepared in anaerobic conditions.

Crystal structures of the complexes.

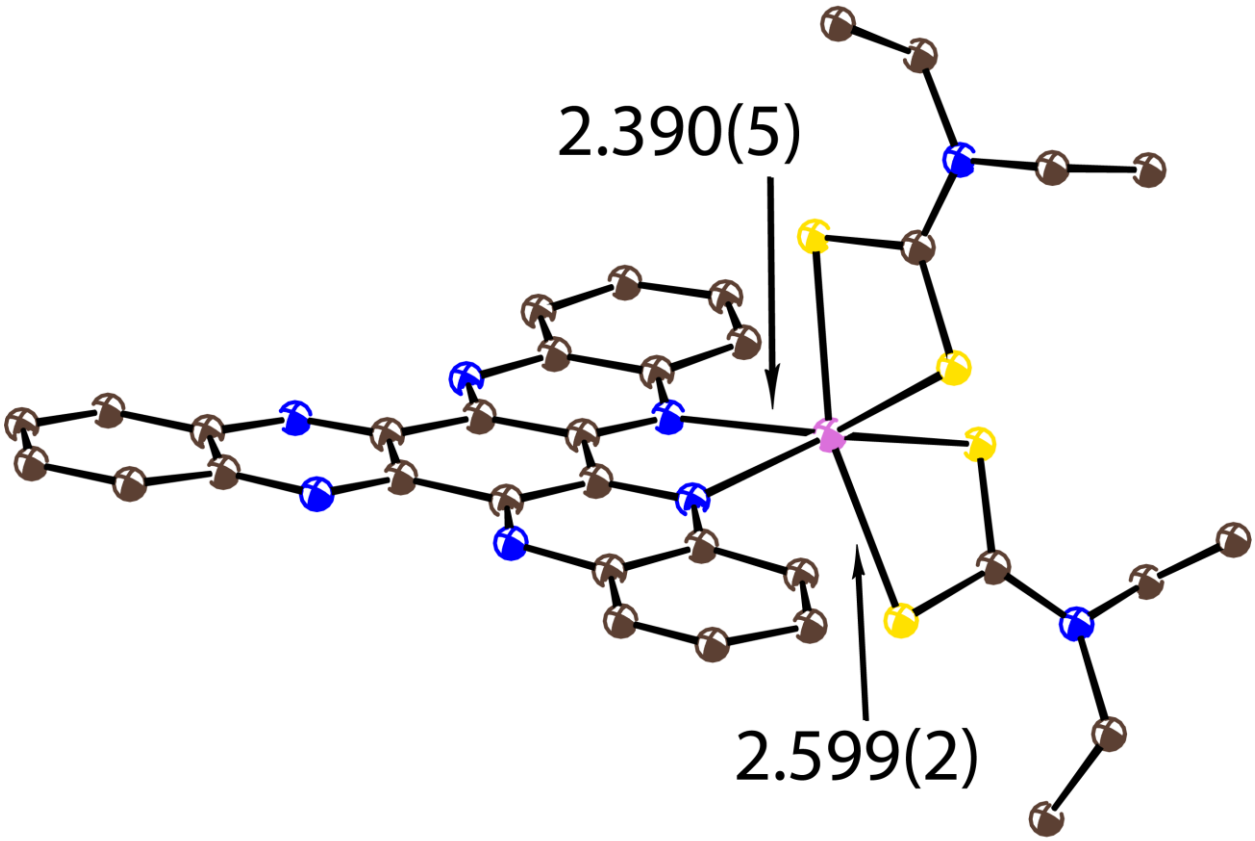

Figure S4. Molecular structure of [{$Mn^{II}(dedtc)_2$}(HATNA)] in **1**. The lengths of the Mn-N and Mn-S bonds are shown. Ortep drawing with equivalent isotropic atomic displacement parameters is shown. Carbon is brown, nitrogen is blue, manganese is pink, sulfur is yellow.

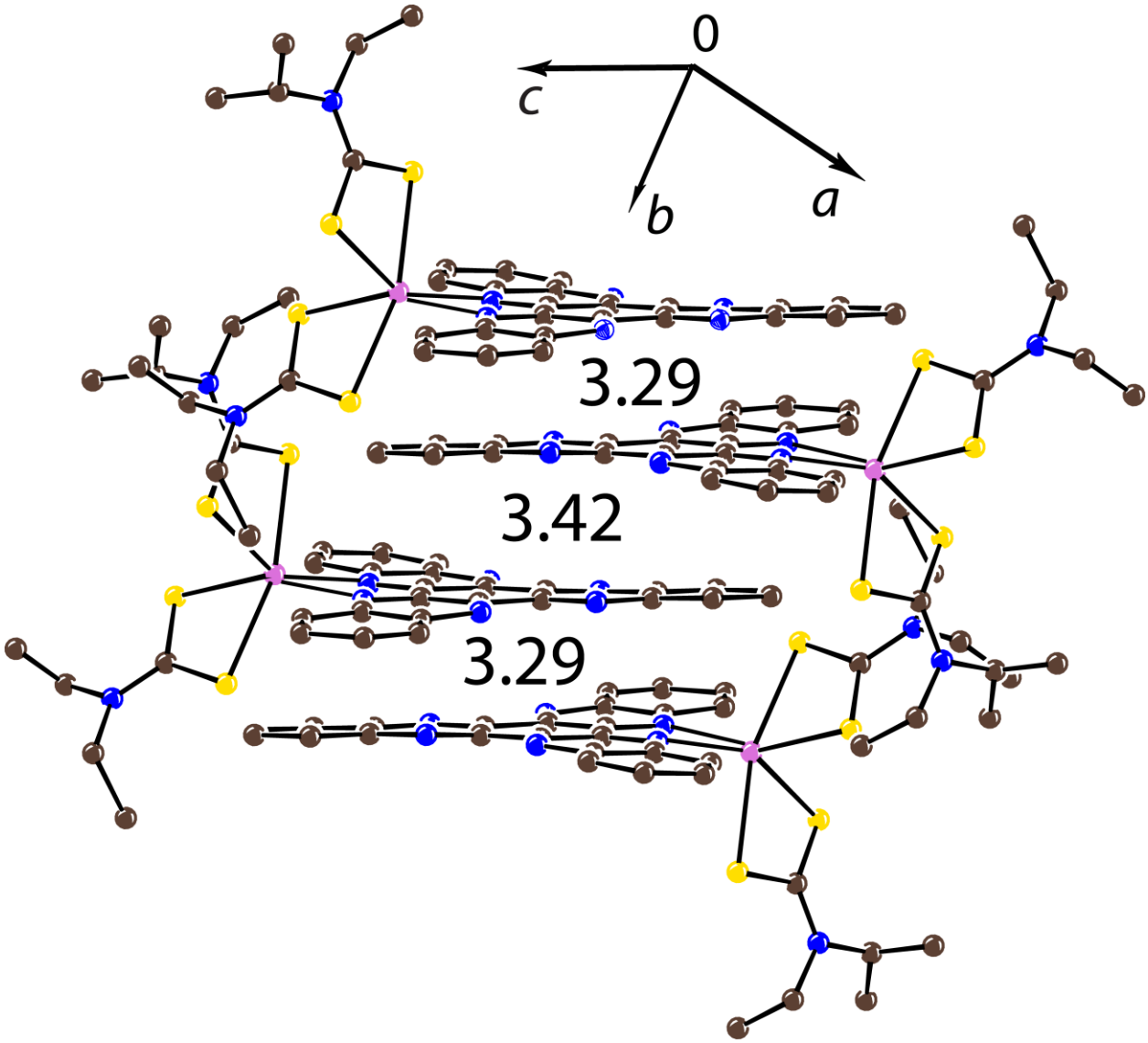

Figure S5. Crystal structure of **1**: view in the stacks from the HATNA molecules together with the interplanar distances is shown. Ortep drawing with equivalent isotropic atomic displacement parameters is shown. Only major occupied orientation is shown for ethyl-substituents of dtc. Carbon is brown, nitrogen is blue, manganese is pink, sulfur is yellow.

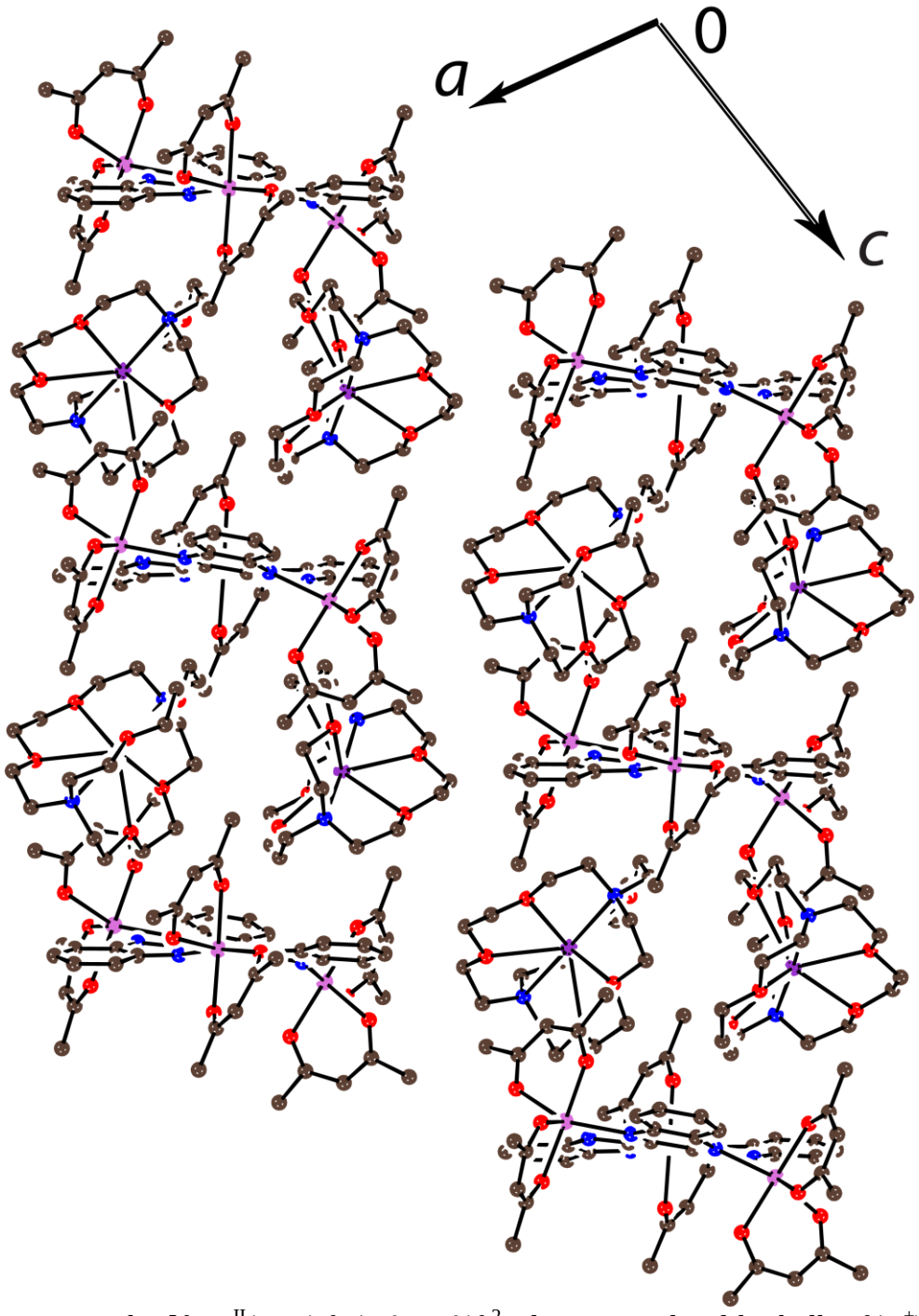

Figure S6. View on the $[\{Mn^{II}(acac)_2\}_3(HATNA)\}^{2-}$ dianions isolated by bulky $\{(K^+)(crypt)\}$ cations in **3** is shown. Solvents $C_6H_4Cl_2$ and C_6H_{14} molecules are not shown for clarity. Ortep drawing with equivalent isotropic atomic displacement parameters is shown. Carbon is brown, nitrogen is blue, manganese is pink, oxygen is red.

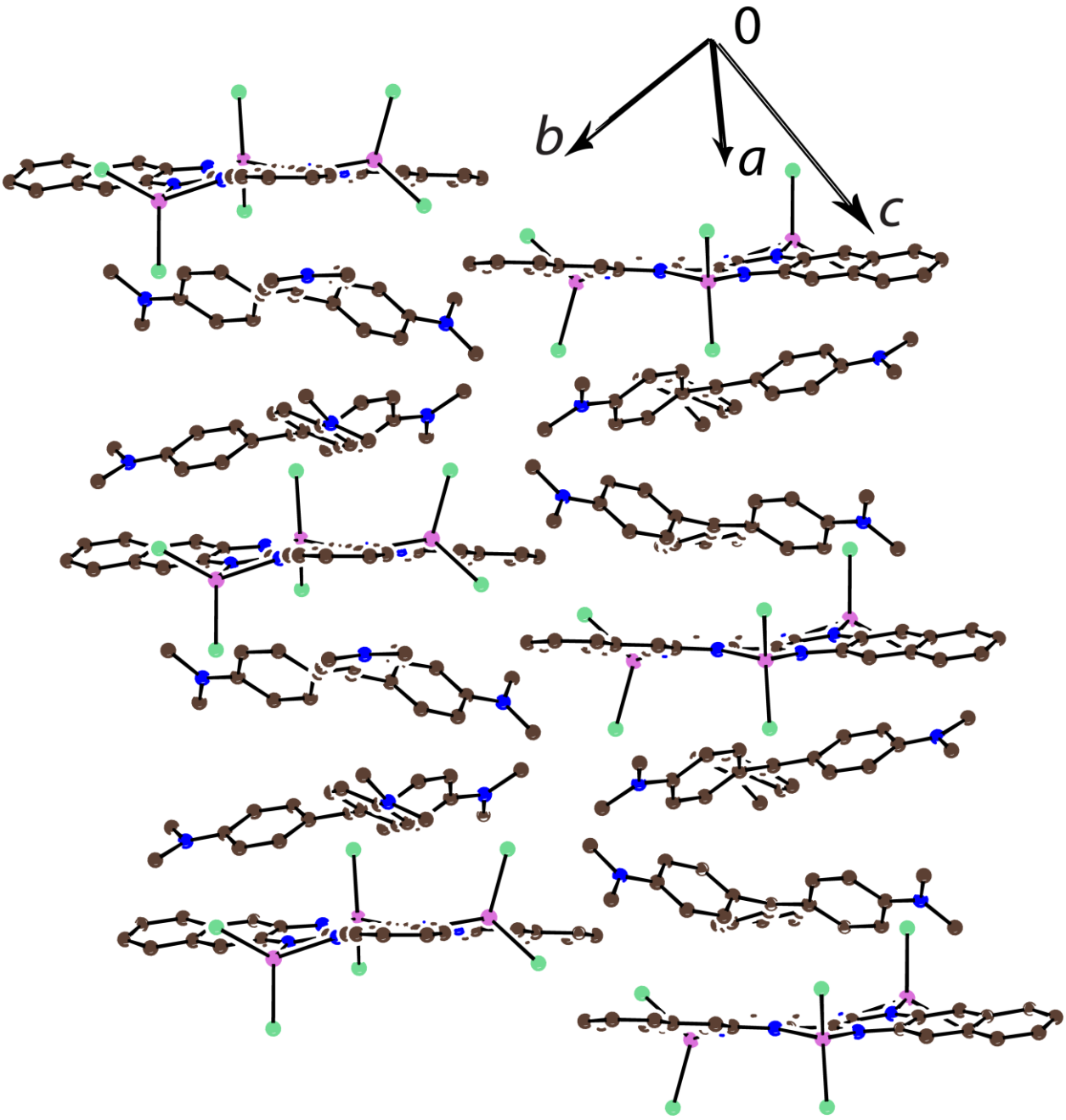

Figure S7. View on the $\{(Mn^{II}Cl_2)_3(HATA)\}^{2-}$ dianions in **4** separated by two CV^+ cations is shown. Solvents $C_6H_4Cl_2$ molecules are not shown for clarity. Ortep drawing with equivalent isotropic atomic displacement parameters is shown. Carbon is brown, nitrogen is blue, manganese is pink, chlorine is green.

Table S3. Shape analysis of the metal complexes **1**-**5** using SHAPE 2.1 software. The smaller value is, the closer geometry of the coordination polyhedron of a metal center gets to the perfect one. Non-equivalent manganese atoms are labeled as Mn^n.

Complexes	Reference polyhedra				
	Hexagon (D_{6h})	Pentagonal pyramid (C_{5v})	Octahedron (O_h)	Trigonal prism (D_{3h})	Johnson pentagonal pyramid (C_{5v})
Mn (**1**)	26.415	19.842	13.038	15.526	20.964
	Hexagon (D_{6h})	Pentagonal pyramid (C_{5v})	Octahedron (O_h)	Trigonal prism (D_{3h})	Johnson pentagonal pyramid (C_{5v})
Mn^1 (**2**)	26.410	17.038	12.903	7.527	20.643
Mn^2 (**2**)	29.961	18.998	13.722	11.205	20.611
Mn^3 (**2**)	25.700	16.856	13.102	7.368	20.344
	Hexagon (D_{6h})	Pentagonal pyramid (C_{5v})	Octahedron (O_h)	Trigonal prism (D_{3h})	Johnson pentagonal pyramid (C_{5v})
Mn^1 (**3**)	26.892	23.896	7.047	11.656	25.674
Mn^2 (**3**)	29.168	21.816	9.353	17.089	23.218
Mn^3 (**3**)	26.637	18.376	11.426	16.532	19.719
	Square (D_{4h})	Tetrahedron (T_d)	Seesaw (C_{2v})	Vacant trigonal bipyramid (C_{3v})	-
Mn^1 (**4**)	21.013	14.205	13.964	11.057	-
Mn^2 (**4**)	31.117	15.057	12.092	13.002	-
Mn^3 (**4**)	33.767	18.396	10.485	12.111	-
	Square (D_{4h})	Tetrahedron (T_d)	Seesaw (C_{2v})	Vacant trigonal bipyramid (C_{3v})	-
Mn^1 (**5**)	26.989	13.041	6.670	11.209	-
Mn^2 (**5**)	30.517	17.154	15.506	12.294	-
Mn^3 (**5**)	31.925	15.864	14.715	10.383	-

Fitting of magnetic data by PHI.

Spin Hamiltonians $\hat{H}_1$ for **2** and **4** and $\hat{H}_2$ for **5**, respectively:

$$\hat{H}_1 = -2J \cdot \sum_{i \neq j}^{i,j \in \{1,2,3\}} \hat{\vec{S}}_i \cdot \hat{\vec{S}}_j + D \cdot \sum_{i=1}^{3} (\hat{S}_{zi}^2 - \frac{1}{3} \cdot \hat{\vec{S}}_i^2) + \mu_B g_{Mn} \sum_{i=1}^{3} \hat{\vec{S}}_i \cdot \vec{H}$$

$$\hat{H}_2 = -2J_1 \cdot \sum_{i=1}^{3} \hat{\vec{S}}_i \cdot \hat{\vec{S}}_4 - 2J_2 \cdot \sum_{i \neq j}^{i,j \in \{1,2,3\}} \hat{\vec{S}}_i \cdot \hat{\vec{S}}_j + D \cdot \sum_{i=1}^{3} (\hat{S}_{zi}^2 - \frac{1}{3} \cdot \hat{\vec{S}}_i^2) + \mu_B (g_{Mn} \sum_{i=1}^{3} \hat{\vec{S}}_i + g_{HAT} \hat{\vec{S}}_4) \cdot \vec{H}$$

where $\hat{\vec{S}}_1$, $\hat{\vec{S}}_2$, and $\hat{\vec{S}}_3$ denote the Mn^{II} spins, $\hat{\vec{S}}_4$ denotes the $HATNA^{\bullet 3-}$ trianionic radical spin, J_1 denotes the Mn^{II}–$HATNA^{\bullet 3-}$, J and J_2 denote Mn^{II}–Mn^{II} exchange values, respectively, g_{Mn} is the Mn^{II} g-factor, and g_{HAT} is the $HATNA^{\bullet 3-}$ g-factor (fixed at 2.0).

Magnetic data for 2.

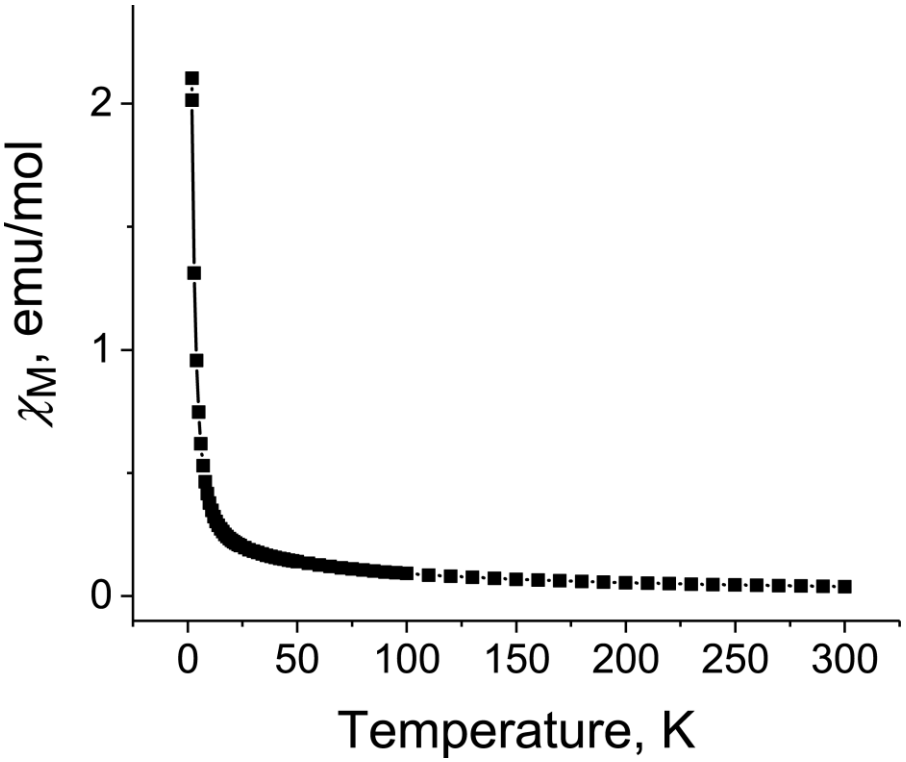

Fig. S8. Temperature dependence of molar magnetic susceptibility of polycrystalline **2** in the 1.9-300 K range.

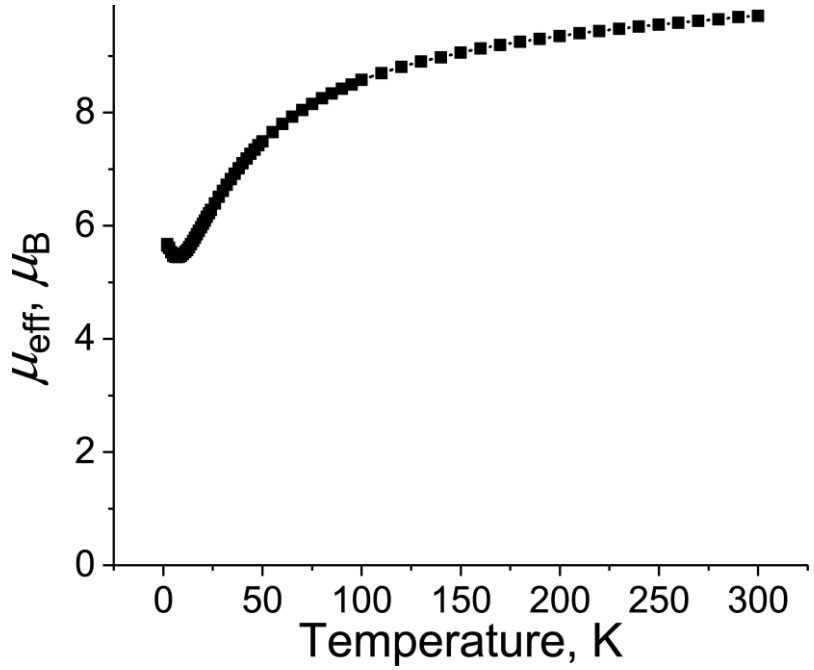

Fig. S9. Temperature dependence of effective magnetic moment of polycrystalline **2** in the 1.9-300 K range.

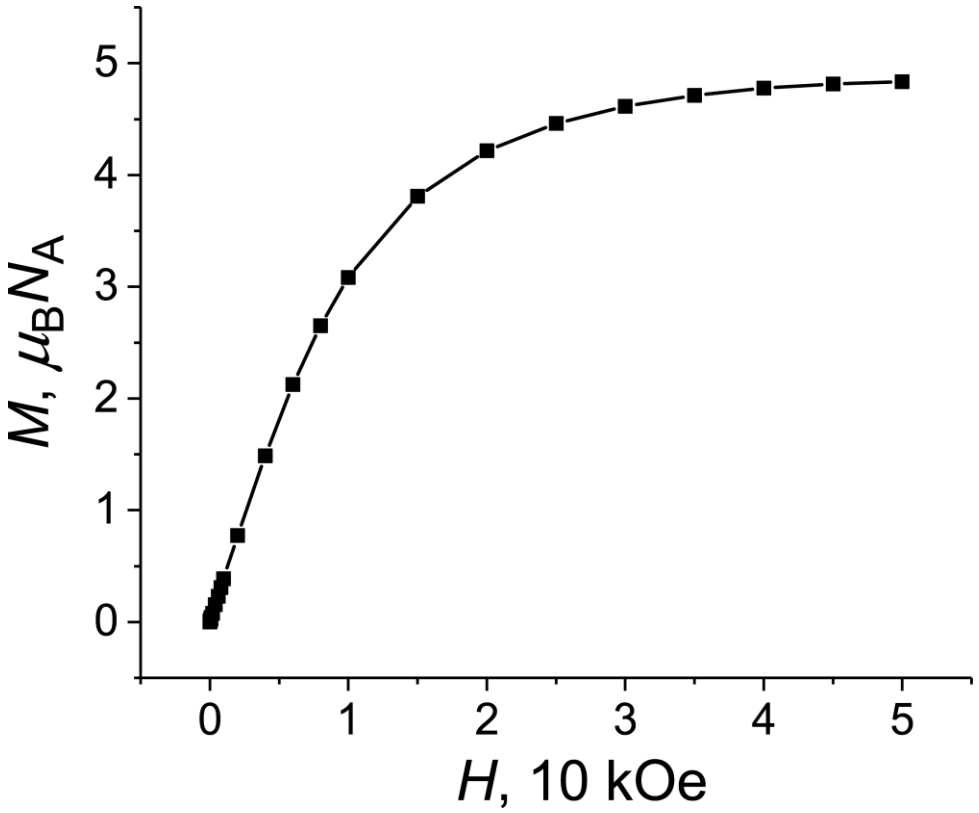

Fig. S10. Dependence of magnetization of polycrystalline **2** *vs* magnetic field up to 5 kOe magnetic field at 2K (black line is a guide to the eye).

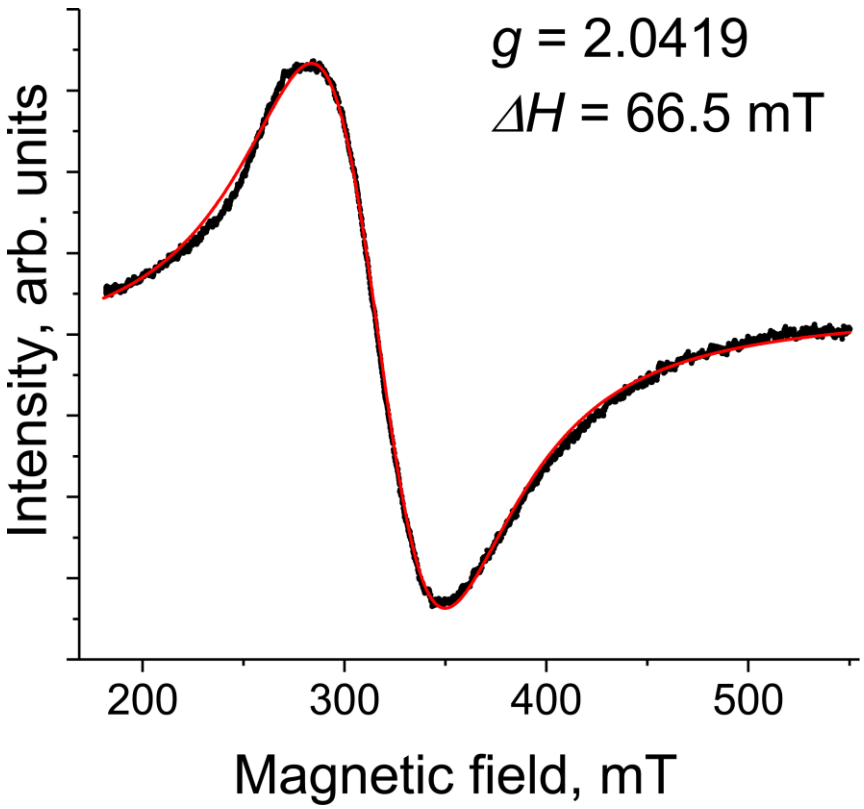

Fig. S11. Isotropic EPR signal from polycrystalline **2** at 100 K.

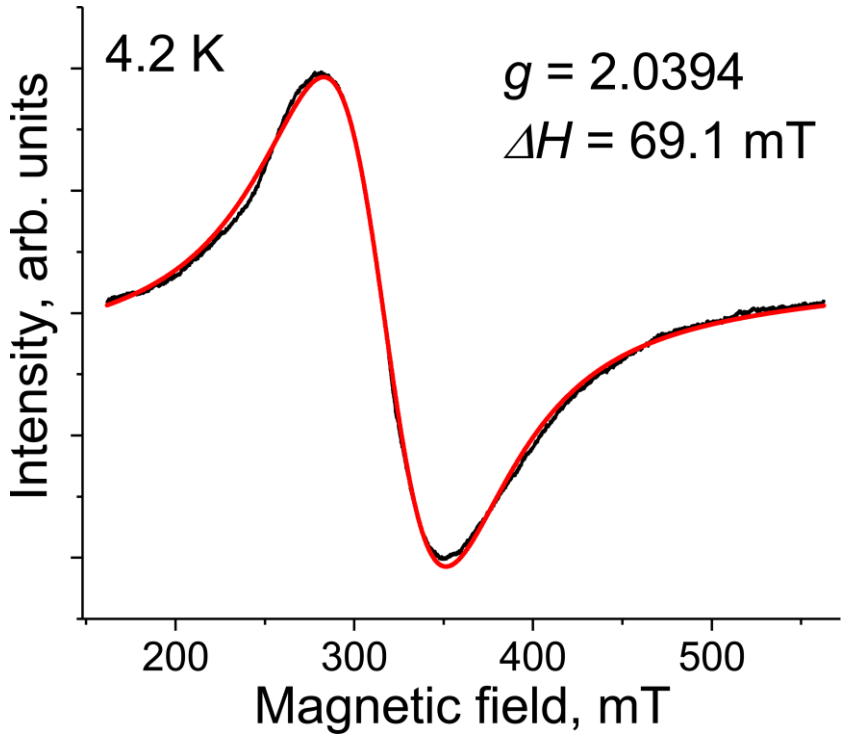

Fig. S12. Isotropic EPR signal from polycrystalline **2** at 4.2 K.

Magnetic data for 4.

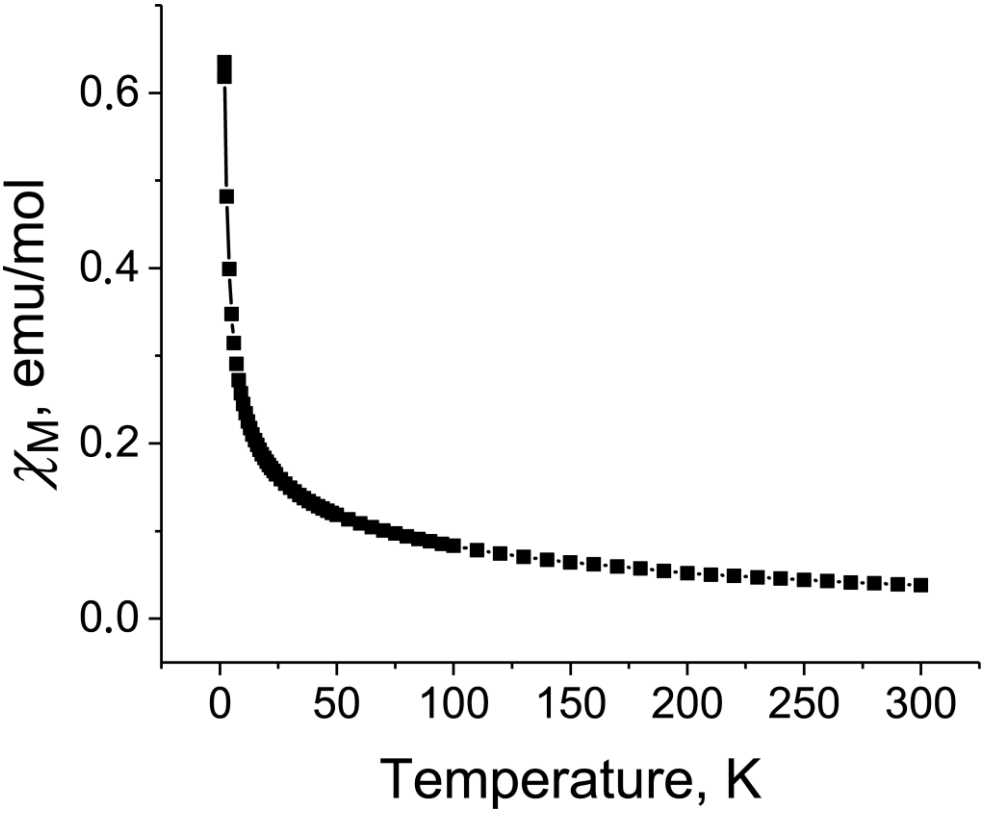

Fig. S13. Temperature dependence of molar magnetic susceptibility of polycrystalline **4** in the 1.9-300 K range.

.

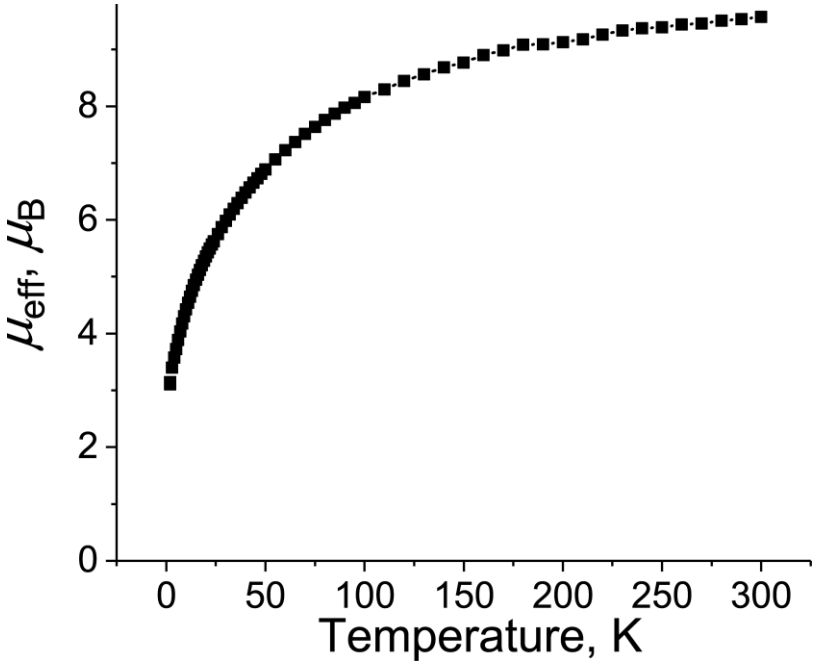

Fig. S14. Temperature dependence of effective magnetic moment of polycrystalline **4** in the 1.9-300 K range.

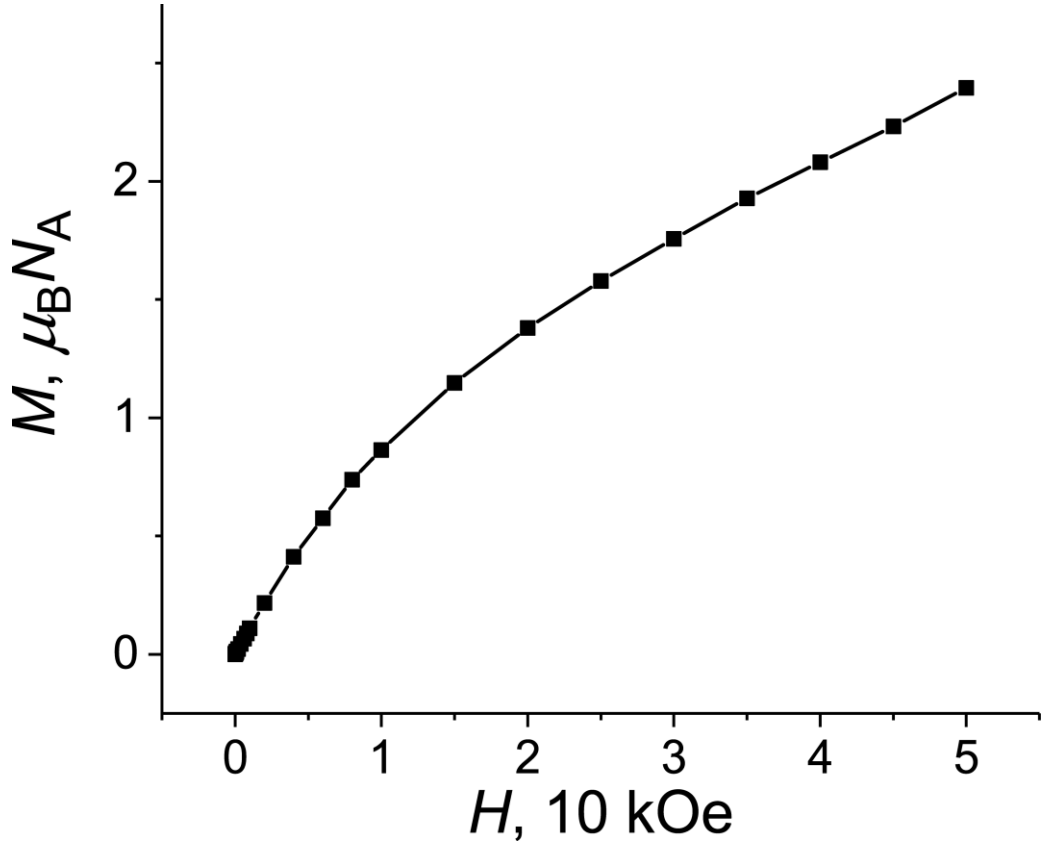

Fig. S15. Dependence of magnetization of polycrystalline **4** *vs* magnetic field up to 5 kOe magnetic field at 2K (black line is a guide to the eye)

.

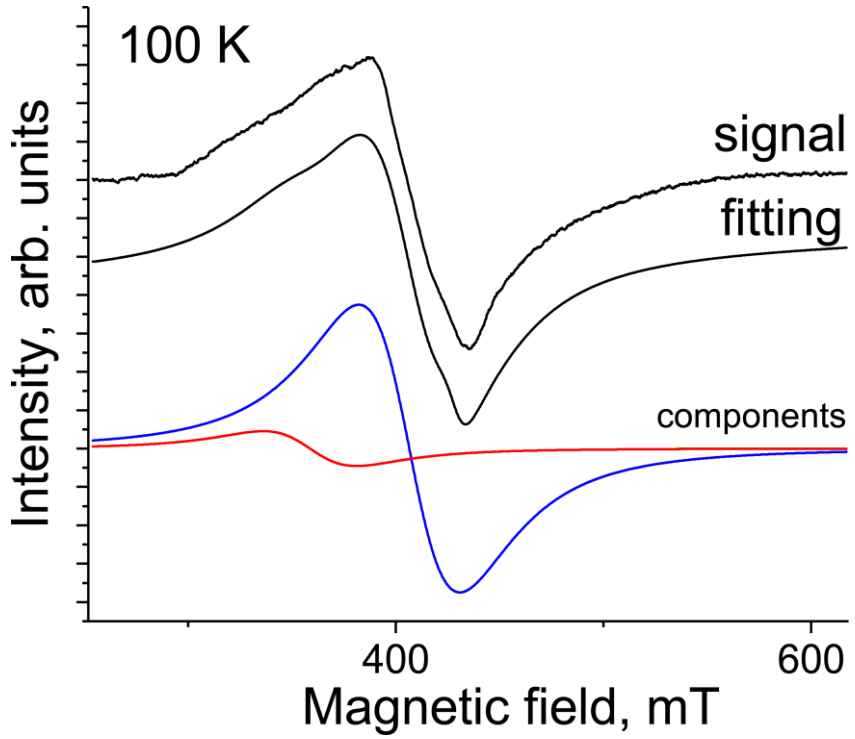

Fig. S16. EPR signal from polycrystalline **4** at 100 K.

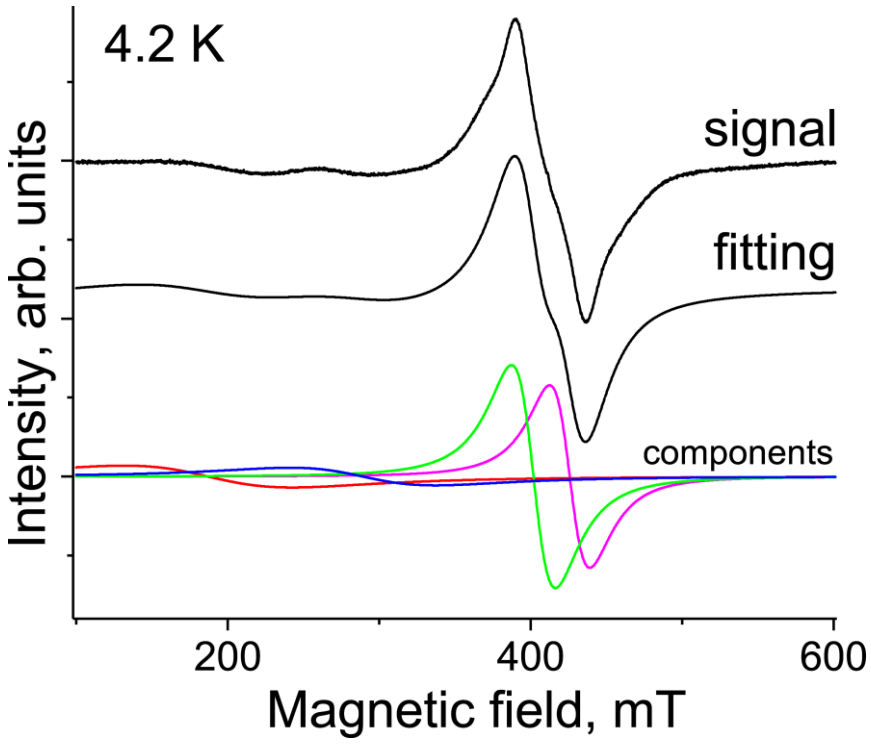

Fig. S17. EPR signal from polycrystalline **4** at 4.2 K.

Magnetic properties of 5.

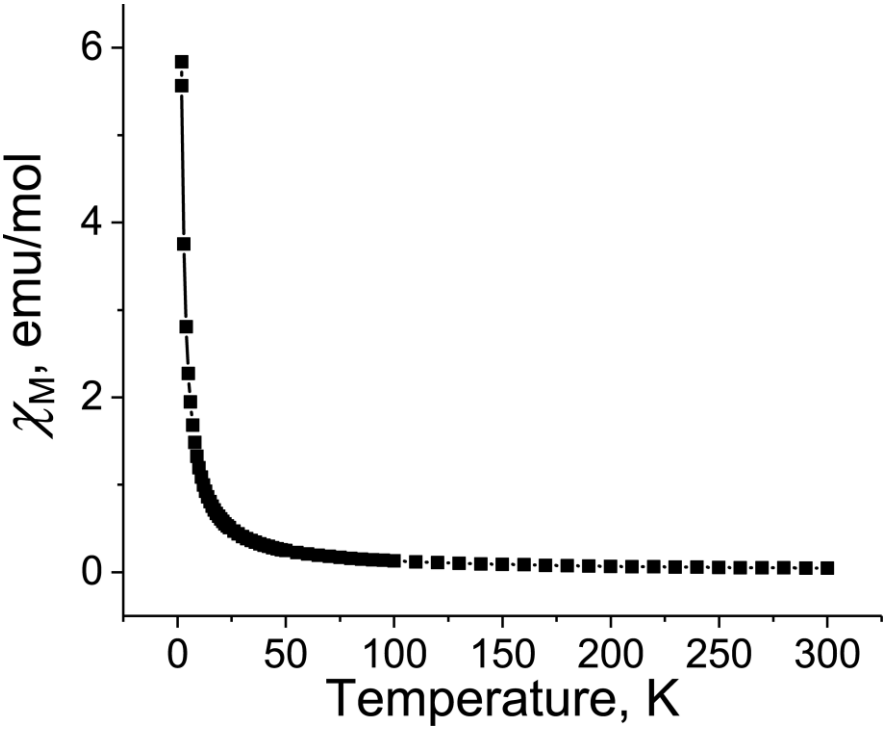

Fig. S18. Temperature dependence of molar magnetic susceptibility of polycrystalline **5** in the 1.9-300 K range.

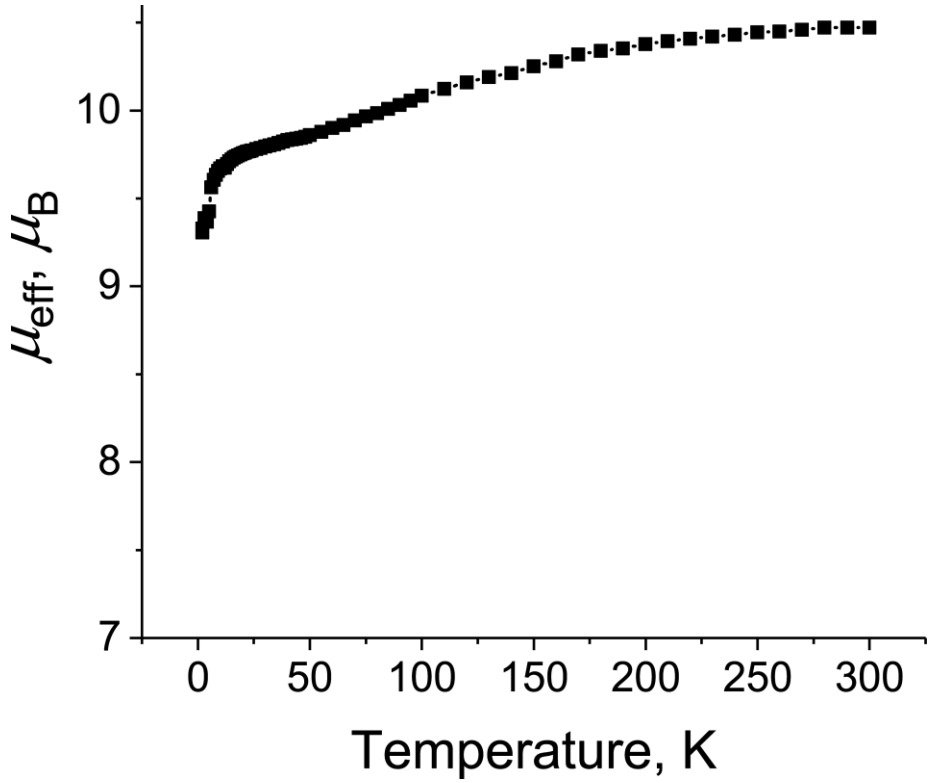

Fig. S19. Temperature dependence of effective magnetic moment of polycrystalline **5** in the 1.9-300 K range.

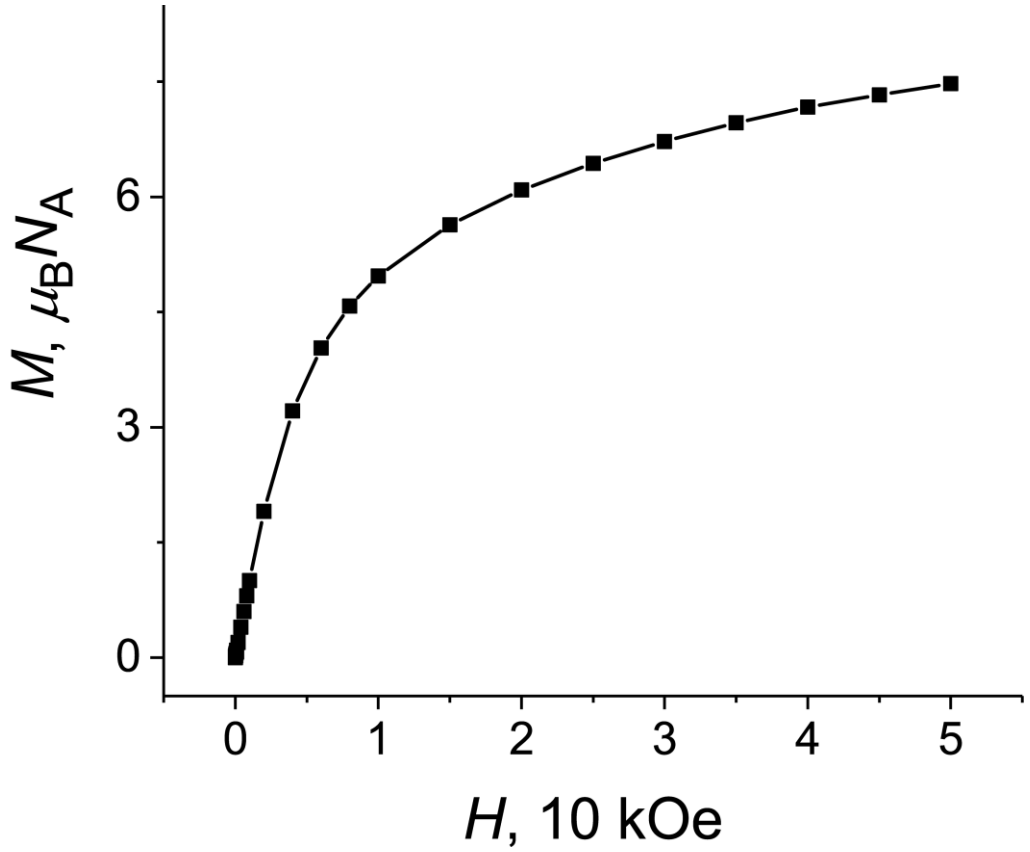

Fig. S20. Dependence of magnetization of polycrystalline **5** *vs* magnetic field up to 5 kOe magnetic field at 2K (black line is a guide to the eye)

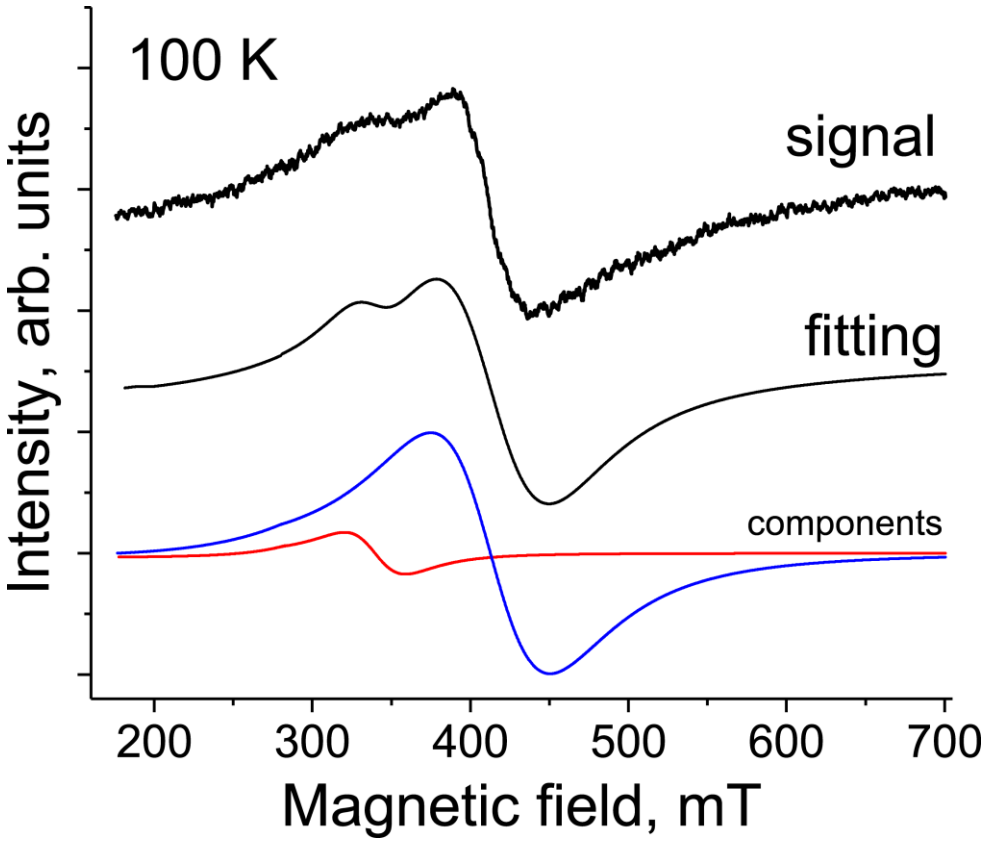

Figure S21. EPR signal from polycrystalline sample of **5** measured at 100 K.

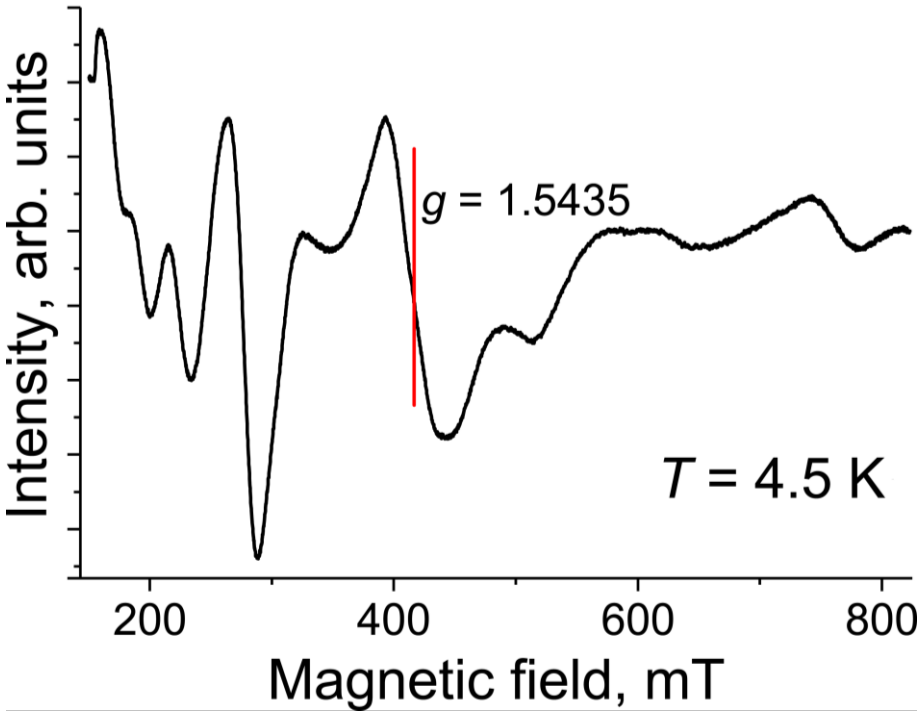

Figure S22. EPR signal from polycrystalline sample of **5** measured at 4.5 K.